Engineering Fracture Mechanics xxx (xxxx) xxx

Contents lists available at ScienceDirect

Engineering Fracture Mechanics

journal homepage: www.elsevier.com/locate/engfracmech

A graph-theoretic approach for multiscale modeling and prediction of crack propagation in polycrystalline materials

Siddhartha Srivastava [a,*], Mohammadreza Yaghoobi [b], Veera Sundararaghavan [a]

[a] Department of Aerospace Engineering, University of Michigan, Ann Arbor, MI 48109, United States of America
[b] Department of Materials Science and Engineering, University of Michigan, Ann Arbor, MI 48109, United States of America

ARTICLE INFO

Keywords:
Fracture
Crack path
Polycrystals
GraphCut

ABSTRACT

A multiscale graph theory-based approach is introduced here to predict the microscale crack path in polycrystalline materials. The crack path is represented as the boundary of the partition of a geometric graph. The partitioning is carried out by optimizing an Ising-type hamiltonian. The hamiltonian parameters are chosen such that each partition cost is the same as the energy of the corresponding crack. The interplay of the loading conditions on the specimen and the microstructure of the material near the crack tip determines the crack growth angle in polycrystalline materials. Two different length scales of macro and micro is incorporated for the crack path by defining the crack total energy as the summation of macroscopic energy release and microscopic surface energy. The former term represents the macroscopically favorable crack growth angle by directing the crack to propagate from the crack tip along the direction of the maximum energy release. The latter term guides the microscopic crack path along the macroscopically preferred direction. At this scale, the crack path naturally accommodates both the intergranular and transgranular fractures. In the case of intergranular fracture, the crack propagates along the grain boundaries, while in the case of transgranular fracture, the crack propagates along the crystallographic cleavage planes. The mixed-mode fracture in a thin foil specimen is studied, and the effect of the dihedral angle of the 2D crack is included in defining the effective surface energy. The model is validated using the analytical results for mixed-mode fracture in an isotropic medium and mode-I fracture in a medium with a preferred crack direction. The proposed method can be used to design materials microstructure with optimal fracture resistance.

1. Introduction

The past two decades have seen extensive development in computational capabilities for graph partitioning. It is especially evident in energy minimization-based methods where metaheuristic schemes, like GraphCut [1], and NISQ era hardware, like Quantum annealers [2], promise the approximation of the globally optimal solution of an NP-hard problem in polynomial time. This development has mobilized researchers to identify classical mechanics problems that can be formalized in the framework of graph theory and be solved with some computational advantage. One such area is the fracture mechanics of polycrystalline materials, where the detailed simulation of cracks is computationally challenging due to the length scale separation in the microstructure and the specimen size. Experimental investigation of crack propagation at this scale is highly time-consuming and complex, and the results demonstrate a considerable variation, which can be attributed to the microstructure-dependent nature of crack initiation. Accordingly, developing the computational tool is crucial to guide and inform the experimental procedures.

* Corresponding author.
E-mail addresses: sidsriva@umich.edu (S. Srivastava), yaghoobi@umich.edu (M. Yaghoobi), veeras@umich.edu (V. Sundararaghavan).

https://doi.org/10.1016/j.engfracmech.2020.107406
Received 4 August 2020; Received in revised form 28 October 2020; Accepted 8 November 2020
Available online 10 November 2020

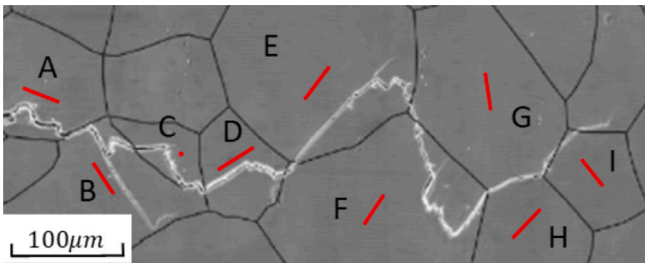

Fig. 1. Experimental image of a fatigue crack in WE43 Mg alloy (HCP) adapted from [18]. Transgranular fracture followed the basal trace (red line) in grains A-F. Intergranular fracture occurred between grain pairs (A,B), (G,H) and (G,I). (For interpretation of the references to color in this figure legend, the reader is referred to the web version of this article.)

Traditionally, the two main types of fractures considered at the microscale are brittle and ductile. In brittle failure, the metal fractures with little to no plastic deformation, generating surfaces with bright cleaved crystalline facets. The crystallographic planes of the microstructure play an essential role in the mechanism of fracture. For instance, at low temperatures, BCC-Iron (Body centered cubic) cleaves on the {001} family of planes and HCP-Zinc (Hexagonal close packed) cleaves on the basal plane, while FCC (Face-centered cubic) materials are usually immune to such failure. In contrast, fracture in ductile failure is preceded by significant plastic deformation, which redistributes the stress concentration ahead of the crack tip, resulting in different fracture mechanisms. The same kind of material can undergo ductile or brittle depending on the external conditions. One of the earliest pioneering studies of transition from brittle to ductile was carried out by Kelly, Tyson, and Cottrell [3]. They proposed that the ratio of the largest tensile stress and the largest shear stress close to the crack tip governs the crack behavior. A brittle fracture occurs when this ratio exceeds the ratio of ideal cleavage stress and the ideal shear stress.

There are two popular approaches in the literature for the numerical simulation of fracture. The first one is based on cohesive zone models [4–7]. These methods have proven to be extremely useful in predicting both the nucleation and crack propagation; however, they are plagued by numerical instabilities. These problems have been mitigated, to a certain degree, using either more stable but computationally extensive load path-following procedures (e.g., Riks method and arc-length method) or by introducing artificial viscosity to the cohesive zone law [8] leading to inaccuracies in load prediction. The second approach is based on Phase-field methods, where cracks are represented using diffuse damage parameters. The evolution of these damage parameters can be modeled using a Ginzburg–Landau type potential [9,10] or using gradient damage theory [11]. There is also the issue of mesh dependence in numerical crack path prediction. It has been shown, for instance, in [12], one of the major reasons for mesh dependence is the stress concentration at the tip. Consequently, mesh-dependent objects like element size near the crack tip can influence the direction of crack growth. These problems are usually addressed using regularization approaches to limit the sensitivity of damage evolution to the stress concentration. Most phase-field studies (for e.g. [11,13]) use regularization by considering a diffused crack. Moreover, many FEM techniques now allow generating sophisticated crack paths like the node enrichment FEM (e.g. X-FEM) [14] and elemental enrichment FEM (e.g. E-FEM) [15,16].

One of the major drawbacks of these approaches is that the solution may not lead to a global minimum of energy due to the problem's non-convex nature. This aspect of the global and local solutions can be better understood in the variational model of quasistatic crack evolution proposed by Francfort and Marigo [17]. Consider the following energy of a body with a given crack, Γ, and external load, U:

$$E(\Gamma, U) = E_d(\Gamma, U) + \int_{\Gamma} 2\gamma ds$$

where E_d is the bulk energy of the body, and γ is the surface energy density of the cracked surface. The crack path is estimated using an evolution law where the load is monotonically increased, and the crack progresses in the direction of a maximum decrease in energy. However, this evolution does not need to lead to a global minimizer of energy. In fact, it is mentioned in [17] that these evolution laws are dependent on the load history and have meaningful continuum limits only in certain conditions. At the same time, the reader is cautioned that this not an endorsement of global energy minimization over local growth law in terms of thermodynamic arguments. The global energy minimization is a postulate which seems crucial in understanding the effect of inhomogeneity of surface energy in polycrystalline materials. As an example, an experimental image for crack propagation in WE43 Mg alloy specimen presented in [18] (see Fig. 1) revealed a crack path which did not propagate completely in the basal direction. Transgranular fracture path in Grain E shows an unusual bending before hitting the grain boundary. A possible explanation is that the intergranular fracture between the grains G and H lowers the overall energy of the crack and therefore influences the crack path in the transgranular region of grain E and F. In comparison, the numerical study of grain boundary effect on the crack path presented in [13] shows this upstream influence at a much smaller length scale. Such results motivate the search for global minimizers of total energy.

On the other hand, graph-based approaches are posed as combinatorial optimization problems with finite choices where, in some instances, the global minimum can be approximated reasonably quickly. In regards to fracture mechanics, such approaches have been employed in predicting fracture at the microscale. Sundararaghavan and Srivastava [19] developed MicroFract, a graph

theory-based software to predict the microstructural crack path in various materials. They validated their model by simulating the intergranular stress corrosion cracking of Inconel. Srinivasan et al. [20] used machine learning along with graph theory to substitute demanding computations with coarse-scale graphs. Hunter et al. [21] also incorporated machine learning along with graph theory and developed reduced-order models, which have sufficient accuracy and low computational cost, to capture brittle fracture. Recent machine learning techniques for fracture prediction have been reviewed in [22]. Needleman and coworkers [23,24] have developed a model based on discrete unit events along with graph theory to predict intergranular fracture in polycrystalline metals. They investigated the effect of grain size on the propagation of ductile intergranular fracture. There is no graph-theoretic approach that can simulate microscale cracks in polycrystals, including intergranular and transgranular cracks, to the best of authors' knowledge.

This paper aims to introduce a general and modular framework for multiscale modeling of a polycrystalline material using a graph-based technique. The macroscopic energy release and the microscopic surface energy, depending on the loading condition and the crystallography of the material, respectively, are encoded into an Ising-type hamiltonian. The non-local component of the hamiltonian (Smoothing term) is obtained as a metric, and therefore, the energy minimization is carried out using the Alpha-expansion method, which guarantees that the min-cut is within a known factor of the global minimum (Kolmogorov and Zabih [25]; Boykov and Kolmogorov [26]). Consequently, the energy of the predicted crack is very close to the globally optimal crack path. The presented scheme can model the crack propagation in mixed-mode-I-mode-II failure in a reasonable time with sufficient accuracy. Furthermore, the algorithm reduces to a Quadratic Unconstrained Binary Optimization (QUBO), which can be solved using quantum annealing systems, like D-wave. A new scheme is developed to incorporate the dihedral angle of cracks in fracture, which considers the effective surface energy of a uniformly oriented out-of-plane crack. The techniques presented here are specialized for brittle fracture in elastic materials. The key idea of this work to represent the fracture energy using the Ising model can be extended to ductile materials, but no such attempt is made in this paper.

The paper is organized as follows: Section 2 develops the formulation for the total energy of the crack in a multiscale setting and relates it to the Ising hamiltonian of the graph. A procedure to estimate the 2D surface energy of 3D crystals is also presented in this section for studying fracture in thin-film specimens. In Section 3, the algorithmic details are described, and a discussion on the computational complexity of the method is presented. In Section 4 the procedure is applied to capture crack paths in two cases : (i) homogeneous media with an anisotropic surface energy and (ii) polycrystalline material. The results for crack growth in homogeneous media are compared against the analytical result. In the case of the polycrystalline material, a qualitative verification of results is presented. The effect of the grain boundary on the crack path is studied, and it is shown that at high loading conditions, the predicted crack path resembles the dynamic fracture path. Section 5 provides a summary of the paper.

2. Mathematical framework

Among the early energy-based methodologies for studying fracture in linear-elastic isotropic materials, the most noted ones are the S-Criterion (Strain Energy Criterion) [27,28] and the ME-Criterion (Maximum energy release rate criterion) [29]. It was first shown in [30] and later proved in [29] that the ME-criterion is the same as Maximum-Stress Theory [31] i.e., the crack propagates in the direction of maximum circumferential stress. For this reason, the ME-criterion is often favored over the S-Criterion for crack angle prediction in mixed-mode failure. The basic hypothesis for ME-Criterion is that:

1. The crack propagates from the crack tip in a straight line along which the maximum energy is released.
2. The crack propagates when the energy release rate is greater than a critical value.

Consider a small kink from the original main crack tip at an angle, α with the horizontal axis. The application of the ME-Criterion to estimate of the propagation angle can be formalized as:

$$\max_{\alpha} G(\alpha) \geq G_c \tag{1}$$

where $G(\alpha)$ denotes the energy release rate for a kink angle, α, and G_c denotes the critical energy release rate. In the case of an ideal brittle fracture, $G_c = 2\gamma$, where γ is the surface energy density of the fractured surface. Now, consider a circular region around the main crack tip determined by the radius, $\bar{r}$, of the branched crack and a microscopic crack path, Γ, parameterized as $\Gamma(s) \equiv (x(s), y(s))$. In this region, the ME-Criterion can be equivalently written in terms of the total energy released (instead of the energy release rate) as follows:

$$\min_{\Gamma} \int_{\Gamma} (2\gamma - G)\, ds \leq 0$$

The above equation was derived by using the fact that G_c, or equivalently, γ is independent of α, which is true for isotropic materials. However, at the microscale, γ depends on the location and the local orientation of the cracked surface. Consequently, the minimizer of this functional is not necessarily a straight line, as postulated in the first hypothesis of the original ME-criterion. Moreover, the second hypothesis is also violated as the equivalent G_c changes with the kink angle. In favor of a multiscale approach, the energy release rate is assumed to be governed by the macroscopic feature of the crack, i.e., kink angle, defined as the average angle of the microscopic crack. The assumptions considered in the new hypothesis for multiscale crack propagation are stated as:

1. Crack, Γ propagates from the crack tip in a possibly zig-zag direction towards the circular region's circumference so that the path minimizes the total energy of the system, $\varepsilon(\Gamma)$:

$$\varepsilon(\Gamma) = \int_{\Gamma} 2\gamma ds - G(\alpha_{\Gamma})$$

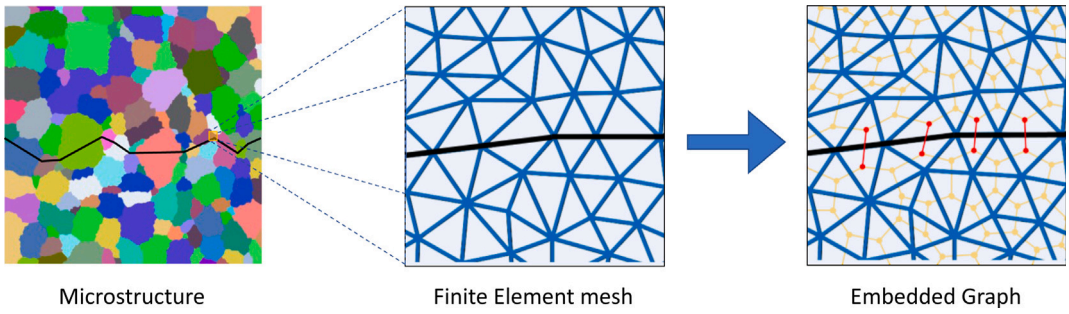

Fig. 2. A portion of the FE mesh (in blue) with the dual graph, G (in yellow) embedded in the mesh. Only the connections across the crack (in red) contribute to the cost. The energy of the connection between elements A and B is determined by the length and the normal of the interface edge. (For interpretation of the references to color in this figure legend, the reader is referred to the web version of this article.)

2. Crack propagation is initiated when the total energy is negative.

The energy release rate for mixed mode crack in isotropic material is estimated in [29] as follows:

$$G(\alpha) = \frac{\kappa+1}{8\mu}\cos^2\frac{\alpha}{2}\left(\cos^2\frac{\alpha}{2}K_{II}^2 + \left(\cos\frac{\alpha}{2}K_I - 2\sin\frac{\alpha}{2}K_{II}\right)^2\right) \tag{2}$$

where κ is a material constant, which can be obtained as $\kappa = 3-4\nu$ for the plane strain condition and $\kappa = (3-\nu)/(1+\nu)$ for the plane stress condition. The variables, μ and ν are the shear modulus and Poisson's ratio for the homogenized material, respectively. Note that the energy release rate for a general anisotropic material [32] can be substituted here without influencing the formulation.

2.1. Graph representation of microscopic crack

A random finite element mesh is considered (see Appendix A for definition) where each element is a polygon represented by P_i with $i \in \{1,\dots,n\}$. The goal is to label each element as $+1$ or -1 based on a cost minimization criterion. Therefore, a particular partition of a mesh is given by an array of labels, $L = [l_1,\dots,l_n]$ with $l_i \in \{+1,-1\}$. The crack is represented as the element edge with different labels on either side. To define the energy of this partition, an undirected graph (see Appendix A for definition) is embedded in this mesh. Each element, P_i, is treated as a vertex, v_i, of the graph, $\mathcal{G}$. A connection, e, exists between two vertices if their respective elements share an edge.[1] This cost is determined as the Ising hamiltonian, H_I, on the graph, $\mathcal{G}$, defined as:

$$H_I(L) = \sum_{v_i\in V} g(c_i,l_i)|P_i| + \sum_{(v_i,v_j)\in E} 2\gamma(\vec{n})\Delta s_{ij}(1-\delta_{l_i-l_j}) \tag{3}$$

where $g(.,+1)$ and $g(.,-1)$ are continuous functions defined over the domain. c_i and $|P_i|$ are the centroid and the area of the element, P_i, respectively. Δs_{ij} and $\vec{n}$ are the length and a unit normal to the interface between the elements, P_i and P_j, respectively. δ_x is the Dirac-delta function, i.e. it has value 1 at $x = 0$ and 0 everywhere else. The function γ is strictly positive and represents the surface energy density of the crystal. It can be immediately observed that the second term does not contribute towards the cost if the labels of neighboring pair are the same (see Fig. 2).

In the next section, the procedure to encode the total energy as an Ising hamiltonian is presented. The first term in Eq. (3) is used to encode the macroscopic energy release, while the second represents the microscopic surface energy of the crack.

2.2. Graph based modeling of energy release

A semicircular region of radius, $\bar{r}$ can be defined as an area of interest where the macroscopic crack grows from the center to the circumference in a straight line. The net energy release increases linearly with the radius, $\bar{r}$. Moreover, it has functional dependence on the kink angle. To encode this behavior of the energy release, following functional form of g is considered as an ansatz:

$$g(c_i,l_i) = (2-k)\bar{r}^{k-1}\frac{\bar{g}(\theta_i,l_i)}{r_i^k} \tag{4}$$

where, θ_i and r_i define the angular and radial coordinates of the point c_i and $k < 2$ for admissibility. Consider a radial crack at an angle α. To understand this choice of function, g, observe that in the continuum limit of the mesh ($\mathcal{P}_h$ with $h \to 0$), the first term of Eq. (3) can be expanded as (see Appendix B Proposition 1 for proof):

$$\sum_{v_i\in V} g(c_i,l_i)|P_i| = \bar{r}\int_{\alpha}^{\pi/2}\bar{g}(\theta,+1)d\theta + \bar{r}\int_{-\pi/2}^{\alpha}\bar{g}(\theta,-1)d\theta \tag{5}$$

[1] In the subject of Graph theory, this construction is referred to as the weak dual of a primal graph, where the vertices and connections of the primal graph are defined identified as the nodes and the edges of the mesh respectively.

where $\{+1\}$ is the label of upper region and $\{-1\}$ is the label for lower region. Moreover, the above equation represents the negative of the energy release in the continuum limit, i.e.

$$\bar{r}\int_{\alpha}^{\pi/2}\bar{g}(\theta,+1)d\theta+\bar{r}\int_{-\pi/2}^{\alpha}\bar{g}(\theta,-1)d\theta=-\bar{r}G(\alpha) \tag{6}$$

Therefore, the initial ansatz for g satisfies the linear dependence on $\bar{r}$ and angular dependence on the crack angle, α. This integral equation form is satisfied by the following form of $g(.,l_i)$ (see Appendix B Proposition 2 for proof):

$$\begin{aligned}\bar{g}(\alpha,+1)&=G'(\alpha)H(G'(\alpha))+c\\ \bar{g}(\alpha,-1)&=-G'(\alpha)H(-G'(\alpha))+c\end{aligned} \tag{7}$$

where H is the heaviside function and c is given by:

$$c=-\frac{1}{\pi}\left(G\left(-\frac{\pi}{2}\right)+\int_{-\pi/2}^{\pi/2}G'(\theta)H(G'(\theta))d\theta\right)$$

The derivative G' can be estimated from Eq. (2) as:

$$G'(\alpha)=-\frac{\kappa+1}{8\mu}\cos\frac{\alpha}{2}\left(\left(\sin\frac{\alpha}{2}+\sin\frac{3\alpha}{2}\right)\frac{K_I^2}{2}+\left(5\sin\frac{\alpha}{2}-3\sin\frac{3\alpha}{2}\right)\frac{K_{II}^2}{2}-2\cos\frac{3\alpha}{2}K_IK_{II}\right) \tag{8}$$

Moreover, a phenomenological choice of $k=1$ is made in this paper. To understand the reason behind this, consider a rough crack represented using its angular position (α) as a function of the radial position. The following relation holds true in the continuum limit (see Appendix B Proposition 3 for proof):

$$\sum_{P_i\in\mathcal{P}_h}g(c_i,l_i)|P_i|=(k-2)\bar{r}\int_0^1\frac{1}{s^{k-1}}G(\alpha(\bar{r}s))ds \tag{9}$$

Therefore, the parameter k can be used to give different weightage to energy release rate at different radial distances. It can be easily observed that for the given choice of k, the excess energy release rate is weighed uniformly.

2.3. Modeling surface energy

The surface energy density, γ, in Eq. (3) varies spatially and is dependent on the angle of the cracked surface. The treatment of edges between elements of the same grain (transgranular) is done differently from the ones with a distinct grain (intergranular). Here, the energies related to both the crack growth pattern of transgranular and intergranular types are elaborated.

Transgranular surface energy: Transgranular cracks usually prefer propagation along crystallographic planes, typically those with low indices. This effect is due to the relatively smaller energy density for these planes. Due to the symmetry of crystals, the surface energy density also obeys these rules, i.e. for the function γ^{tg} to represent the surface energy density of a crystal system, it must satisfy: $\gamma^{tg}(Q\star\vec{n})=\gamma^{tg}(\vec{n})$, where Q is an element of the group, $\mathcal{G}$, consisting of appropriate symmetry operations, and $Q\star\vec{n}$ denotes the action of Q on $\vec{n}$. These energies are often available in the literature for specific crystallographic planes. The symmetry conditions can then be encoded using appropriate interpolation. This practice is fairly common in smeared crack approaches; for instance, surface energy density interpolation for crystals with cubic symmetry is introduced in [33].

As an example, a model for transgranular surface energy density of a crystal with cubic symmetry is chosen. In this case, $\mathcal{G}$ is the group generated by the operations:

$$\{R_x(\pi/2),R_y(\pi/2),R_z(\pi/2),-I\}$$

where R_x, R_y and R_z are rotations about the chosen coordinate system and $-I$ is the inversion operator. The surface energy density of the crack for a cubic material is modeled as:

$$\gamma^{tg}(\theta,\phi)=\gamma_0\left(1+3\delta\left(\frac{\cos^2\theta\sin^2 2\phi}{4}+\sin^2\theta\right)\cos^2\theta\right) \tag{10}$$

where θ and ϕ are the elevation and the azimuth of the unit normal to the cleavage plane relative to the crystal frame of reference. The $\{001\}$ family of planes has the minimum energy given by the parameter, γ_0, while the $\{011\}$ family has a saddle with energy $\gamma_0(1+3\delta/4)$ and the $\{111\}$ family has a maximum with energy $\gamma_0(1+\delta)$. An illustration of this model is shown in Fig. 3 where the cubic symmetries are evident.

Intergranular surface energy: An intergranular crack propagates via grain-boundaries, and the grain-boundary energy, γ_{GB} determine the surface energy. The effective intergranular surface energy density of the cracked surface, γ^{ig}, is determined as:

$$\gamma^{ig}=\gamma_{\text{surface}}-\frac{1}{2}\gamma_{GB} \tag{11}$$

where γ_{surface} is the average energy required to break atomic bonds per unit surface area of individual grain species. As suggested by the above relation, grain boundaries with lower γ_{GB} are more stable as the surface energy is higher along those grain boundaries. These energies are crucial in modeling crack propagation via special grain-boundaries like the coherent twin boundary (CTB), which has the lowest energy (see Fig. 4)

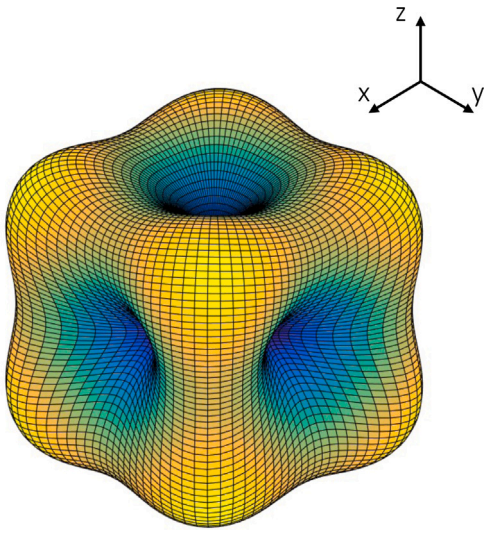

Fig. 3. An illustration of the 3D surface energy density of a cubic material with $\gamma_0 = 1$ J/m^2 and $\delta = 2$ in the direction normal to the cleavage surface.

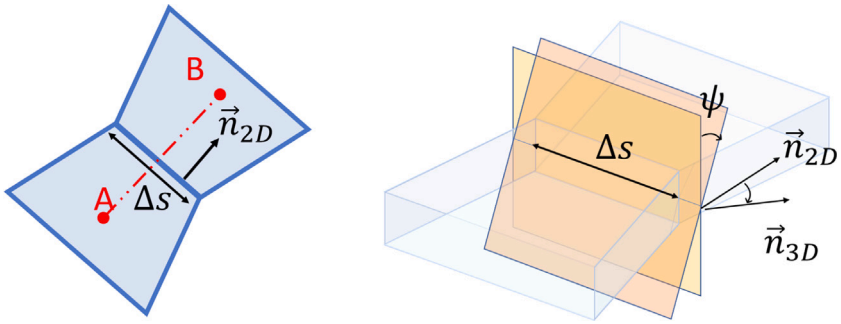

Fig. 4. An illustration for the dihedral angle of a 2D crack.

2.3.1. *Fracture in thin foils*

During crack propagation in these films of crystalline material, unlike isotropic material, the dihedral angle (out of plane angle) cannot be assumed to be zero. Consider a specimen with uniform thickness and a 2D crack that extends in the third dimension with a dihedral angle, ψ_D. Therefore, the surface area generated by a unit 2D crack is $\sec\psi_D$. The dihedral angle is chosen such that the total surface energy is minimized for all possibles dihedral angles. It is also evident that the dihedral angle depends on the direction of the edge. Without a loss of generality, the microstructure surface is chosen to be on the $x_1 - x_2$ plane. The dihedral angle is defined as the angle between the unit normals, $\vec{n}_{2D}$ and $\vec{n}_{3D}$. The general unit normal to the 3D crack can be parameterized with an angle ψ as:

$$\vec{n}_{3D} = [0, 0, 1]^T \sin\psi + \vec{n}_{2D} \cos\psi$$

And the dihedral angle is estimated as:

$$\psi_D = \text{argmin}_{\psi\in(-90°,90°)}\, \gamma\left(\vec{n}_{3D}(\psi)\right) \sec\psi \tag{12}$$

The effective surface energy for the 2D crack is then calculated as:

$$\widetilde{\gamma} = \gamma(\vec{n}_{3D}(\psi_D)) \sec\psi_D \tag{13}$$

The surface energy density and effective dihedral angle for three different grain orientations are shown in Fig. 5 for a cubic material with the surface energy model defined as Eq. (10). It can be observed that cracks with lower surface energy density are possible by considering the dihedral angle.

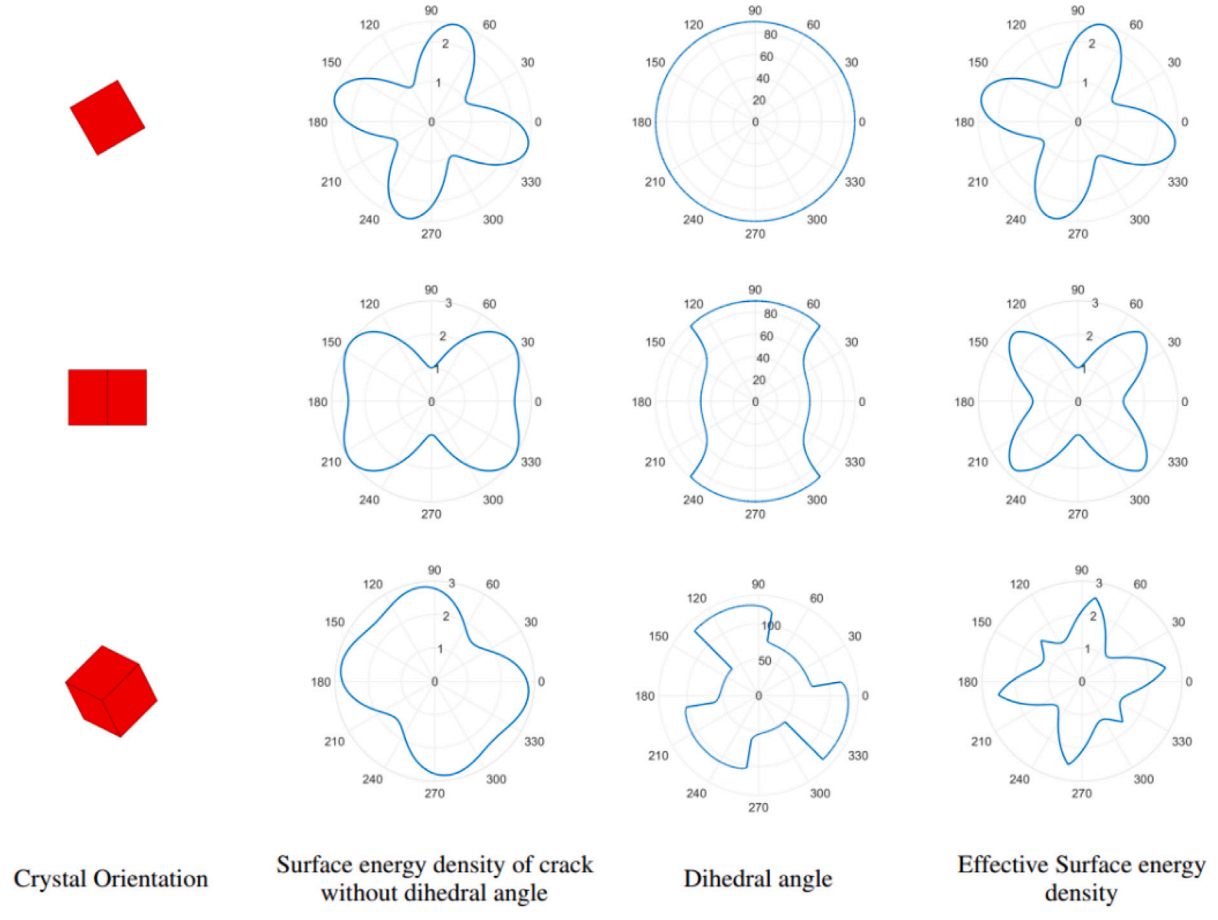

Fig. 5. 2D surface energy density of a cubic material with $\gamma_0 = 1$ J/mm^2 and $\delta = 2$. Each row represents a specific crystal orientation in the specimen frame of reference, and the polar plots are evaluated with respect to cleavage normals. 2D surface energy densities are evaluated for a specimen with unit thickness. The dihedral angle is plotted as $\psi_D + 90°$ for positivity considerations in the polar plot.

3. Method

3.1. Problem setup

A Tensile test is considered with an inclined main crack to replicate the conditions of Mixed mode failure (shown in Fig. 6). The main crack has a half-length, a and an inclination angle, β.

The stress intensity factor can be estimated as:

$$K_I = \sigma_T \sqrt{\pi a} \sin^2 \beta$$
$$K_{II} = \sigma_T \sqrt{\pi a} \sin \beta \cos \beta \tag{14}$$

where σ_T is the applied tensile stress.

3.1.1. Boundary condition

The minimization of Eq. (3) leads to two types of solutions: (1) Both labels are present — This means that there is a crack propagating at an effective angle, $\overline{\alpha} \in (-\pi/2, \pi/2)$ (2) Only one label is present. The latter condition should not be confused with a vertical crack because there is no surface energy being generated in this case. Moreover, due to the lack of surface energy, this erroneous solution's total energy can be substantially low in the absence of a strong directional dependence of the macroscopic energy release rate. For this reason, boundary conditions are applied where the labels $+1$ and -1 are imposed on a thin strip on top and bottom of the main crack-tip (as shown in Fig. 6(b)). It is done by artificially increasing the value determined by the term $g(c_i, -1)|P_i|$ in the top strip and $g(c_i, +1)|P_i|$ in the bottom strip.

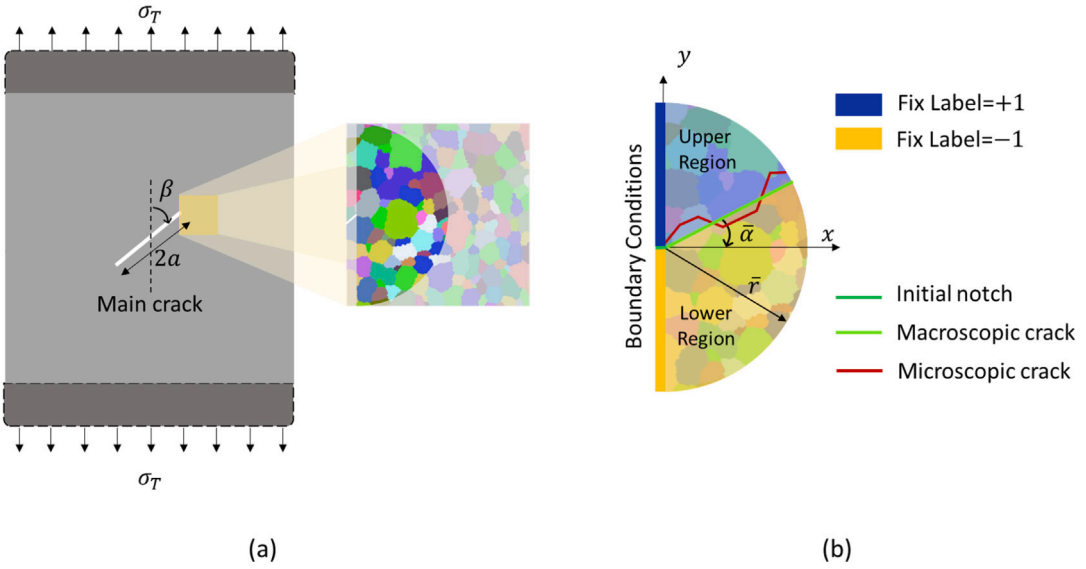

Fig. 6. (a) A tensile test specimen for mixed mode failure (b) The definition of the macroscopic crack angle from the microscopic crack path.

3.1.2. Checking total energy

After enforcing the boundary conditions, the minimization process predicts the crack path as per the Revised ME-Criterion's first hypothesis. However, this procedure does not check whether the total energy is negative; i.e., it violates the second hypothesis. This problem is resolved by checking the total energy after the labeling is done, and the solution is discarded if the total energy is positive.

3.2. Computational procedure

Experimental imaging techniques usually provide a pixelated image with a grain index of each pixel and a table relating grain index to its orientation. This data is superposed on a mesh, which is generated using a Delaunay triangulation of randomly sampled points by determining the grain index of each element using the technique developed in [34]. This method ensures that the grain boundaries in the resulting mesh are smooth. The crack is identified as the boundary between the elements with different labels. This labeling is carried out by minimizing the cost function presented in Eq. (3) using the Alpha-expansion method. The gco library developed by [1] is used to minimize the cost function. This library requires three costs functions namely, label cost, LC, data cost, DC, and neighbor cost, NC. The label cost is given as:

$$LC(i,j) = 1 - \delta_{(l_i - l_j)} = \begin{bmatrix} 0 & 1 \\ 1 & 0 \end{bmatrix} \tag{15}$$

The neighbor cost defines the weight of connection between the ith and jth element, which can be defined as follows:

$$NC(i,j) = 2\gamma(\overline{n})\delta s_{ij} \tag{16}$$

The data cost describes the cost of labeling the jth vertex. It is decomposed as, $DC = DC_0 + DC_{BC}$ where DC_0 denotes the data cost for emulating the macroscopic energy release and is given as

$$\begin{aligned} DC_0(1,j) &= g(\theta_j, +1)|P_j|/r_j \\ DC_0(2,j) &= g(\theta_j, -1)|P_j|/r_j \end{aligned} \tag{17}$$

The term DC_{BC} denotes the data cost used for imposing boundary condition. Taking k as a large constant, the term DC_{BC} is set as $DC_{BC}(1,j) = k$ when the jth vertex is in the bottom strip and $DC_{BC}(2,j) = k$ when the jth vertex is in the top strip. For all other indices, $DC_{BC} = 0$.

A flowchart for the computational procedure is presented in Fig. 7. The list of all the variables and pseudo-codes for all the subroutines are provided in Appendix C. It can be observed that this procedure allows for a unidirectional workflow with (1) Mesh generation (2) Microstructure specific calculation, i.e., identification of grain ID and setting up Neighbor cost (3) Test-specific calculation, i.e., setting up data cost and estimation of the crack. Independence of Step(1) from Step(2) allows using the same random mesh multiple times by re-estimating the Grain index of the mesh for different microstructures. Similarly, the independence of Step(2) from Step(3) relieves the burden of calculation of the Neighbor cost for different loading scenarios on the same microstructure. This effect is achieved by generating the list of indices, $R\text{-}Index$, of the elements in the radial region, and using it to extract the Neighbor Cost of the radial region.

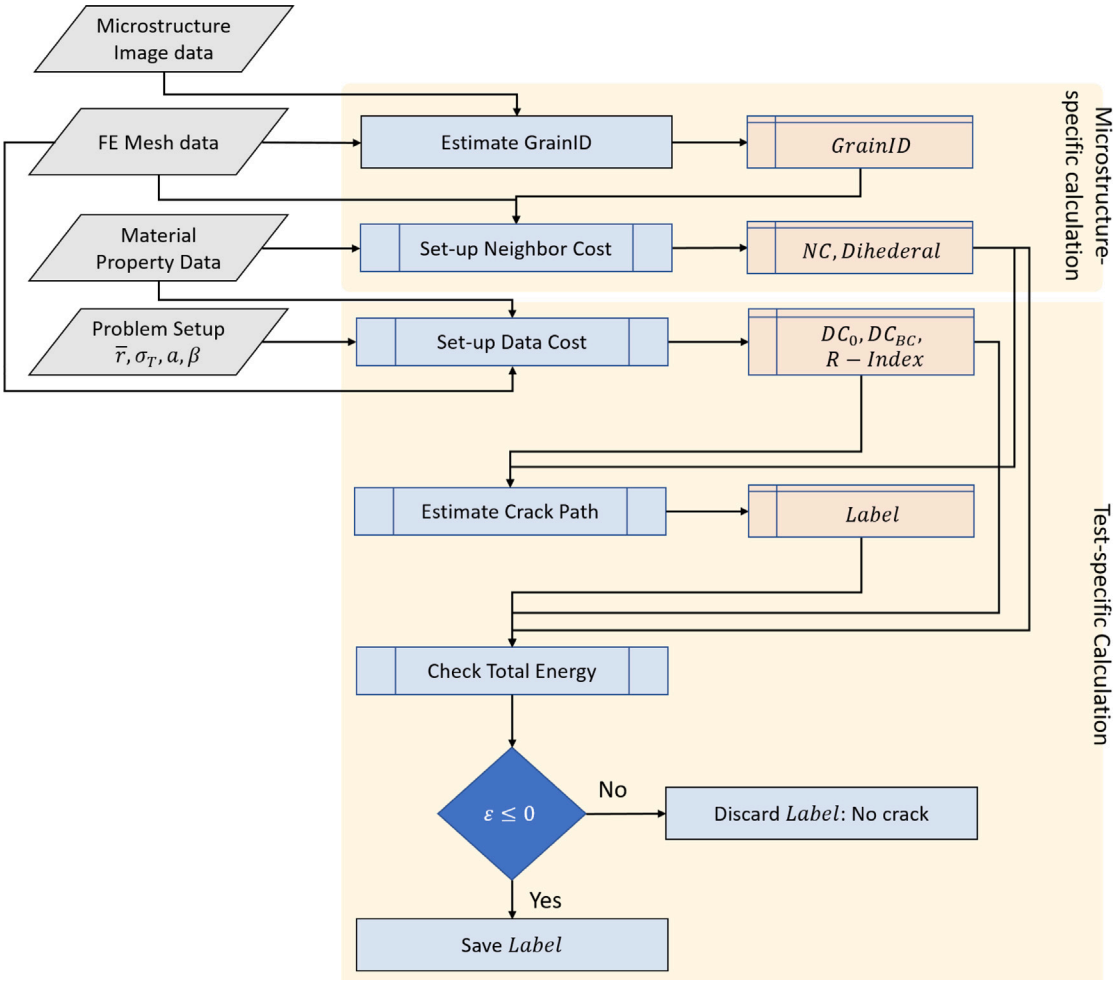

Fig. 7. Flowchart of the procedure for crack estimation.

3.3. Computational complexity

This procedure's total runtime can be estimated as the sum of the individual components of the workflow mentioned above. Before analyzing them separately, it is crucial to understand the resulting graph's topology. The Finite element mesh can also be thought of as a graph with its nodes as the vertices of a graph and the edges as the connections of the graph. Since $\mathcal{G}$ is constructed as a subgraph of a dual of a planar graph (Mesh Graph), it is planar. Based on the construction, the number of vertices, $|V|$ of $\mathcal{G}$ is equal to the number of elements (N) in the mesh. Moreover, the connections, $|E|$ in $\mathcal{G}$ is bounded from above by $3N-6$.

The *Estimate GrainID* subroutine developed in [34] uses a graph with the same topology as used in this work. The main bottleneck in this procedure, as well as the *Estimate Crack Path* procedure, is the GraphCut step. It has been shown in [35], that the runtime complexity for this step is $\mathcal{O}(N \log N)$. The complexity for the *Set-up Neighbor Cost* and *Set-up Data Cost* can be estimated as $\mathcal{O}(|V|)$ and $\mathcal{O}(|E|)$, respectively. Therefore, both the cost setup procedures are $\mathcal{O}(N)$. Finally, the *Check Total Energy* subroutine uses the sparsity of a graph to estimate the cost in $\mathcal{O}(|V|+|E|)$, i.e., it is bounded linearly by N. This analysis shows that the overall runtime complexity of this method is $\mathcal{O}(N \log N)$. The run-time of each process for various mesh-sizes is provided in Fig. 8. It is observed that the *Set-up Data Cost* takes the most computation time for the given choices of the mesh sizes. However, the computation time for *Estimate Crack Path* shows the fastest growth with mesh size.

4. Application to examples

The essential characteristics of the brittle fracture using the proposed formulation are verified in this section. All simulations are conducted for quasistatic crack growth due to the abundance of analytical results in such cases. The quasistatic crack growth condition is replicated by choosing the value of σ_T such that the total energy, ε, is as close to 0 as possible while maintaining non-positivity. The reason for this choice is that, in practice, when the tensile load is increased, the crack propagation initiates as

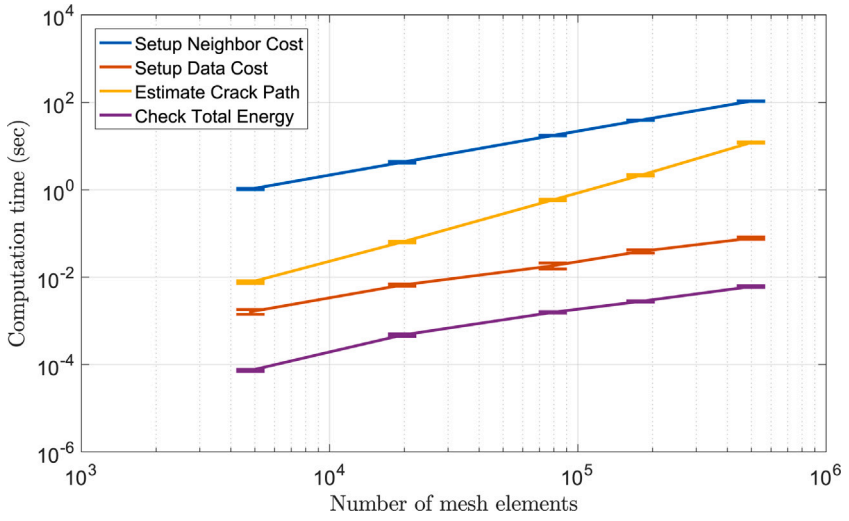

Fig. 8. Run-time Analysis: Computation time is estimated for each process for different mesh sizes. A sample set of 20 meshes is used for each mesh size. Error bars represent the standard deviation in the computation time for each sample set.

soon as the total energy of the crack is negative. The first set of simulations is conducted on a homogeneous material, and the results are verified against analytical results. In the next set of simulations, multiple grains are considered. In this case, analytical results are rare, and the results are analyzed in a qualitative sense. All numerical studies are done on a square domain, discretized into approximately $180k$ elements. Consequently, the complete graph, $\mathcal{G}$, has around $180k$ nodes and $270k$ connections. When restricted to the semicircular simulation domain, the sub-graph contains around $70k$ nodes and $105k$ connections. A mesh convergence analysis is presented in the case study for isotropic fracture (Section 4.1.1) that validates this choice of the mesh size. The radius ($\bar{r}$) of crack-growth region is chosen as half the image's dimension. This hyper-parameter defines the macroscopic length scale of the problem and influences the crack path in the polycrystalline medium. This effect is analyzed in Section 4.2.2.

4.1. Fracture in a homogeneous medium

Homogeneous materials have uniform properties throughout the domain. Three different cases are considered based on the form of surface energy density. In the first case, an isotropic material is studied. Next, a surface energy density with a single preferential direction is considered. Finally, a surface energy density with multiple preferential directions is studied. For simplicity, all the surface energies are formulated for 2D, so the crack's dihedral angle is uniformly zero in all the cases studied here. It should also be noted that the anisotropy is only induced through the surface energy while the energy release rate is based on isotropic material (as defined in Eq. (2)).

4.1.1. Isotropic crack

Firstly, the mesh convergence analysis is conducted using the test case of Mode-I fracture in this medium. The analytical crack grows horizontally while the numerically estimated crack grows in a zig-zag fashion about the horizontal line. The difference between the 'Analytical' and the 'Numerical' crack can be estimated using the Simple matching distance of the corresponding labeling problem. In this case, the distance can be evaluated using the following form:

$$d(C_{\text{Numerical}}, C_{\text{Analytical}}) = 2\frac{\text{Area between}(C_{\text{Numerical}}, C_{\text{Analytical}})}{\pi \bar{r}^2} \tag{18}$$

where, $C_{\text{Numerical}}$ and $C_{\text{Analytical}}$ represent the Numerical and the analytical crack path. An illustration of the area along with the estimated between the two cracks is presented in Fig. 9. It is observed that $d(C_{\text{Numerical}}, C_{\text{Analytical}})$ decreases with an increasing mesh size. The mesh with approximately $180k$ elements is chosen for its reasonable accuracy and computation time.

Next, it is verified that the revised ME-Criterion used in the formulation of the energy minimization problem is, in fact, equivalent to the original ME-criterion for an isotropic material. Erdogan and Sih [31] performed a mixed-mode fracture experiment using plexiglass sheets with oblique cracks under tension. The crack's average angle in their experiments is presented in Table 1. The crack angle, as predicted by the original ME-criterion, is also provided. The numerical simulation using the revised ME-criterion is provided in Fig. 10. The macroscopic crack propagation angle matches reasonably well with the experimental and analytical results.

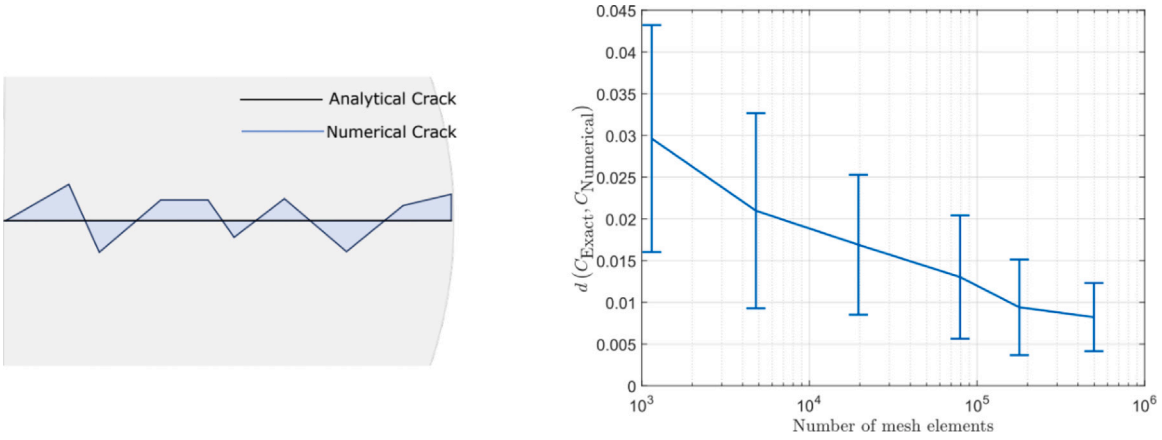

Fig. 9. Mesh convergence analysis: $d(C_{\text{Numerical}}, C_{\text{Analytical}})$ is estimated for different mesh sizes. A sample set of 20 meshes is used for each mesh size. Error bars represent the standard deviation in $d(C_{\text{Numerical}}, C_{\text{Analytical}})$ for each sample set.

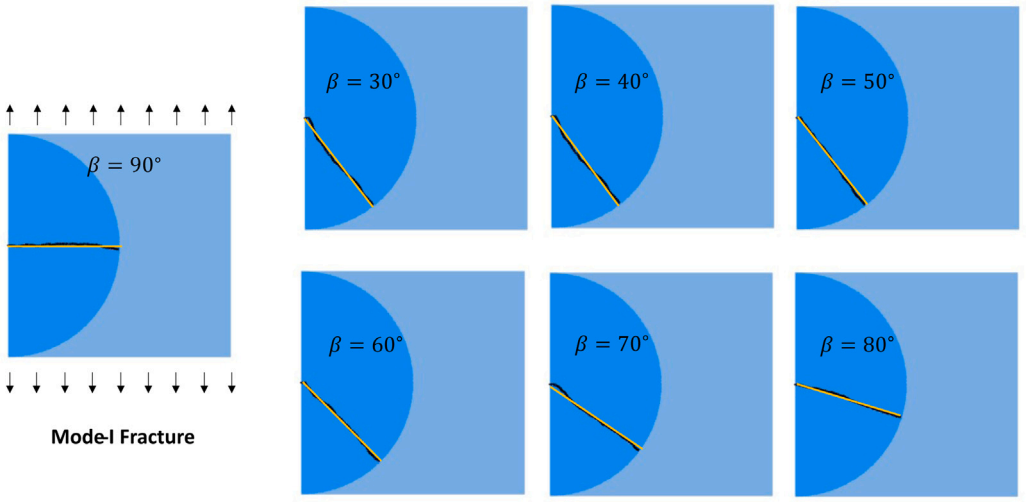

Fig. 10. The crack path predicted in mixed-mode failure of an isotropic media. The black line represents the numerically simulated crack in the semi-circular region. The overlaid yellow line represents the corresponding macroscopic crack direction. (For interpretation of the references to color in this figure legend, the reader is referred to the web version of this article.)

Table 1
Crack propagation angle in mixed-mode failure.

	$\beta = 30°$	$\beta = 40°$	$\beta = 50°$	$\beta = 60°$	$\beta = 70°$	$\beta = 80°$	$\beta = 90°$
Experiment [31]	−62.4°	−55.6°	−51.1°	−43.1°	−30.7°	−17.3°	–
ME-criterion	−60.1°	−55.5°	−50.2°	−43.2°	−33.2°	−19°	0°
Numerical	−62°	−56°	−52°	−43°	−34°	−20°	0°

4.1.2. Single cleavage plane

As the next example, a material with a preferred cleavage direction for the microscopic crack is studied. The surface energy of the crack is low in the prescribed direction of the cleavage plane. The following 2-parameter model for energy function with $\gamma_0, \delta > 0$ is used:

$$\gamma(\theta) = \gamma_0(1 + \delta \cos^2(\theta - \omega)) \tag{19}$$

where θ is the angle of the edge normal and $\omega \in [0, \pi]$ is the preferred direction of the microscopic crack, i.e., the minimum surface energy is generated when the crack propagates along the vector $[\cos\omega, \sin\omega]$. The parameter, γ_0, denotes the preferred cleavage plane's surface energy, and $1 + \delta$ is the ratio of the maximum surface energy to the preferred cleavage plane's surface energy.

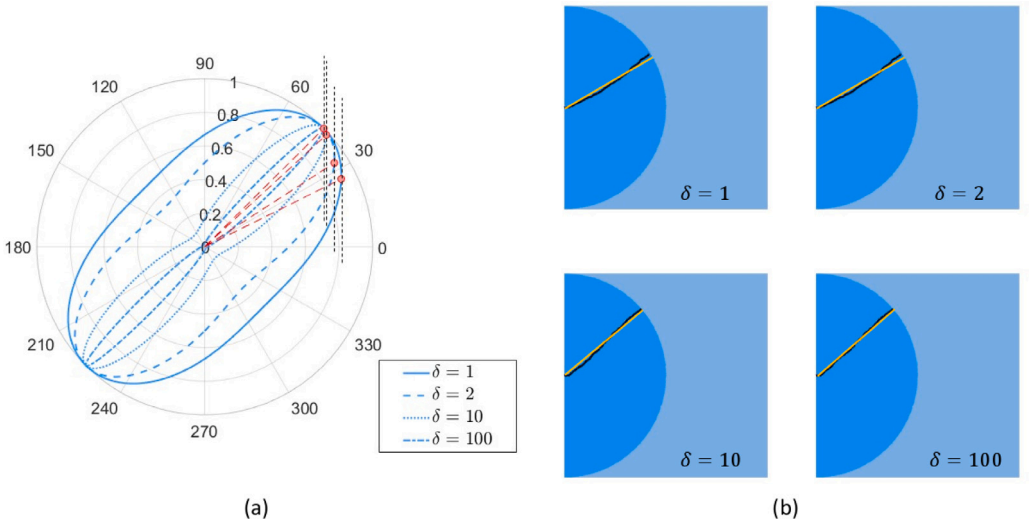

Fig. 11. The crack path predicted in the mode-I failure of a homogeneous media with a preferred cleavage direction of 45°. (a) Polar plot of the surface energy density for different values of δ. (b) Numerically simulated crack where the black line represents the microscopic crack, and the overlaid yellow line represents the corresponding macroscopic crack direction. (For interpretation of the references to color in this figure legend, the reader is referred to the web version of this article.)

Table 2
Crack propagation angle in mixed-mode failure.

δ	1	2	10	100
Analytical [36]	26.4°	35°	42.6°	44.8°
Numerical	28°	31°	40°	42°
$\frac{(\kappa+1)a\pi}{8\mu\gamma_0}\sigma_T^2$	2.7	3.1	5.4	30.8

A horizontal macroscopic crack is preferred in Mode-I failure. However, the microscopic crack prefers an oblique crack with angle, $\alpha = |\omega - 90°|$. The competition between these two effects results in a crack propagating in the direction with the absolute angle less than the one predicted by the surface energy. Takei et al. [36] introduced a Wulff's diagram based criteria to determine the effective angle of the crack. In the case of a differentiable form of surface energy and Mode-I failure, their method can be described as: the crack angle is determined by the point on the γ^{-1} polar plot (with respect to the crack propagation angle) which is tangentially touched by a vertical line moving continuously from right to left. The polar plot of γ_0/γ with respect to the crack propagation angle, $\theta' = \theta + 90°$, is presented in Fig. 11(a) for $\delta = 1, 2, 10, 100$. The analytical values of the crack propagation angle for each δ value, as estimated by the geometric method [36], is presented in the Table 2. Numerical simulations for crack propagation are conducted for each value of delta, and the results are presented in Fig. 11(b), with the numerical value of the effective angle provided in Table 2. The normalized values of σ_T^2 are also provided. The numerically predicted effective angles of propagation match well with the analytically predicted angles. It should be noted that the surface energy in the preferred direction is the same in all cases. However, it can be observed that the critical tensile stress is significantly higher for higher values of δ. There are two reasons behind this discrepancy: (1) The effective angle of the macroscopic crack is at an angle which is different from the preferred cleavage direction, and (2) the effective surface energy is overestimated due to the zig-zag nature of the crack. The former is the desired effect predicted by [36]; however, the latter is due to mesh discretization and is undesirable. To a certain degree, it can be suppressed by using adaptive meshing techniques to iteratively generate a better-suited mesh for each test case based on the predicted crack. However, this step can lead to high computational costs.

4.1.3. Bi-directional preference of cleavage plane

Crystalline solids usually have multiple cleavage directions, and their relative strength, along with their relative orientation to the loading direction, determines the crack path. In this section, the effect of crystal orientation on the crack path in a simplified setting is studied. Consider a material with two cleavage planes perpendicular to each other with equal cleavage energy in a mode-I test. The surface energy of the material can be chosen as follows:

$$\gamma(\theta) = \gamma_0 \left(1 + \delta \sin^2 (2(\theta - \omega))\right)$$

The physical interpretation of the parameters, γ_0, and δ is the same as in the previous case. The preferred direction of the microscopic crack is along the vector $[\cos\omega, \sin\omega]$ and $[-\sin\omega, \cos\omega]$. The polar plot of γ_0/γ is presented in Fig. 12(a, b) for two different values of ω. It was shown by [36] that the regions of local minimum in these polar plots have a neighborhood around them in which

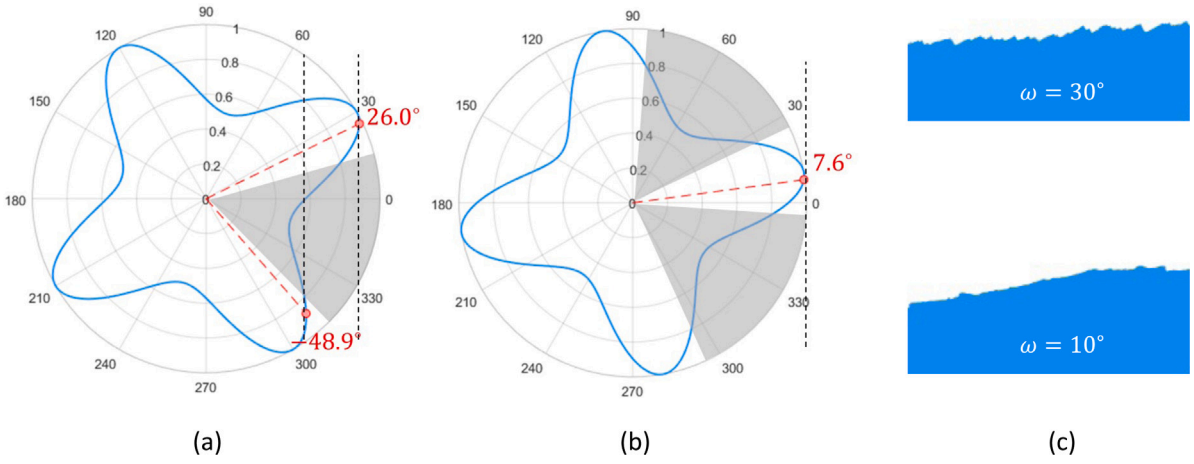

Fig. 12. Polar plot for γ_0/γ with respect to the crack propagation angle, $\theta' = \theta - 90°$ for a bi-directional surface energy with $\delta = 1$ and the crystal orientation (a) $\omega = 30°$, (b) $\omega = 10°$. The gray area represent the forbidden regions (c) The lower region of the cracked surface for $\omega = 30°$ (top) and $\omega = 10°$ (bottom).

the crack never propagates. They referred to these regions as the forbidden regions, which they determined to be the regions of negative curvature in the polar plot. The geometric method based on Wulff's diagram is extended to such cases by determining all the points that have vertical tangents in the polar plot and then removing those in the forbidden region. For instance, in the case of $\omega = 30°$, there are two optimal crack propagation angles, while in the case of $\omega = 10°$ there is only one (as shown in Fig. 12(a, b)) . The existence of such a region implies that in the presence of multiple optimal crack propagation angles with a forbidden region between them, the local orientation of the crack path rapidly switches between these optimal angles to accommodate the microscopically preferred path. The result is a saw-tooth pattern on the cracked surface. The fractured surfaces for $\omega = 30°$ and $\omega = 10°$ as estimated by the method in this paper are shown in Fig. 12(c). The saw-tooth pattern is present in the case of $\omega = 30°$ but absent in $\omega = 10°$ as expected.

4.2. Cracks in polycrystalline material

The presence of multiple grains has two effects: (1) The spatial variation of the preferred cleavage directions, and (2) intergranular fracture along grain boundaries. These effects are qualitatively analyzed in this section. Next, the effect of having non-zero surface energy is studied.

4.2.1. Effect of grain boundary

A bi-crystal in the mode-I fracture is considered in this section, with each grain having a single preferred cleavage plane. Both grains have the same parameters for energy described by Eq. (19) with $\delta = 2$. The bicrystal's geometric construction is such that the grain boundary is a straight line passing through the point $0.25\bar{r}, 0.5\bar{r}$ at an angle, χ, to the horizontal axis. The crystal in the top left corner is labeled Grain 1, and the one in the bottom right corner is labeled as Grain 2. The orientation for Grain 1 is chosen to be $\omega = 0°$, and for Grain 2 is chosen to be $\omega = 45°$. Based on the analysis from Section 4.1.2, the effective crack path angles in the single crystal of Grain 1 and 2 in mode-I fracture are $\alpha = 0°$ and $\alpha \approx 35°$, respectively. Numerical simulations are carried out by prescribing the surface energy of the grain-boundary, γ^{ig}, in the range: $\{0.5\gamma_0, \gamma_0, 1.5\gamma_0\}$ and the boundary angle, χ, in the range: $\{0°, 30°, 60°, 90°\}$. The results from these numerical simulations are presented in Fig. 13.

The key observations from the numerical simulations are as follows:

1. As γ^{ig} increases, the transgranular fracture is preferred over the intergranular fracture. This can be observed from Fig. 13(b) where increasing γ^{ig} from $0.5\gamma_0$ to γ_0 shows the transition from transgranular to intergranular fracture.
2. The influence of the grain-boundary is more prominent when it is aligned closer to the macroscopically preferred crack path. The reason is that the crack path simultaneously minimizes the macroscopic energy release and surface energy. Therefore, the crack switches from transgranular to intergranular when the difference of surface energy compensates for the lower macroscopic energy release.
3. The grain-boundary can influence the crack path before it passes through it. This can be observed in Fig. 13(c) with $\gamma^{ig} = 0.5\gamma_0$. The preferred crack propagation angle in Grain 1 is 0°. However, the lower value γ^{ig} influences the crack to dip downwards to lower the crack's overall surface energy. This result is an artifact of the global energy minimization.

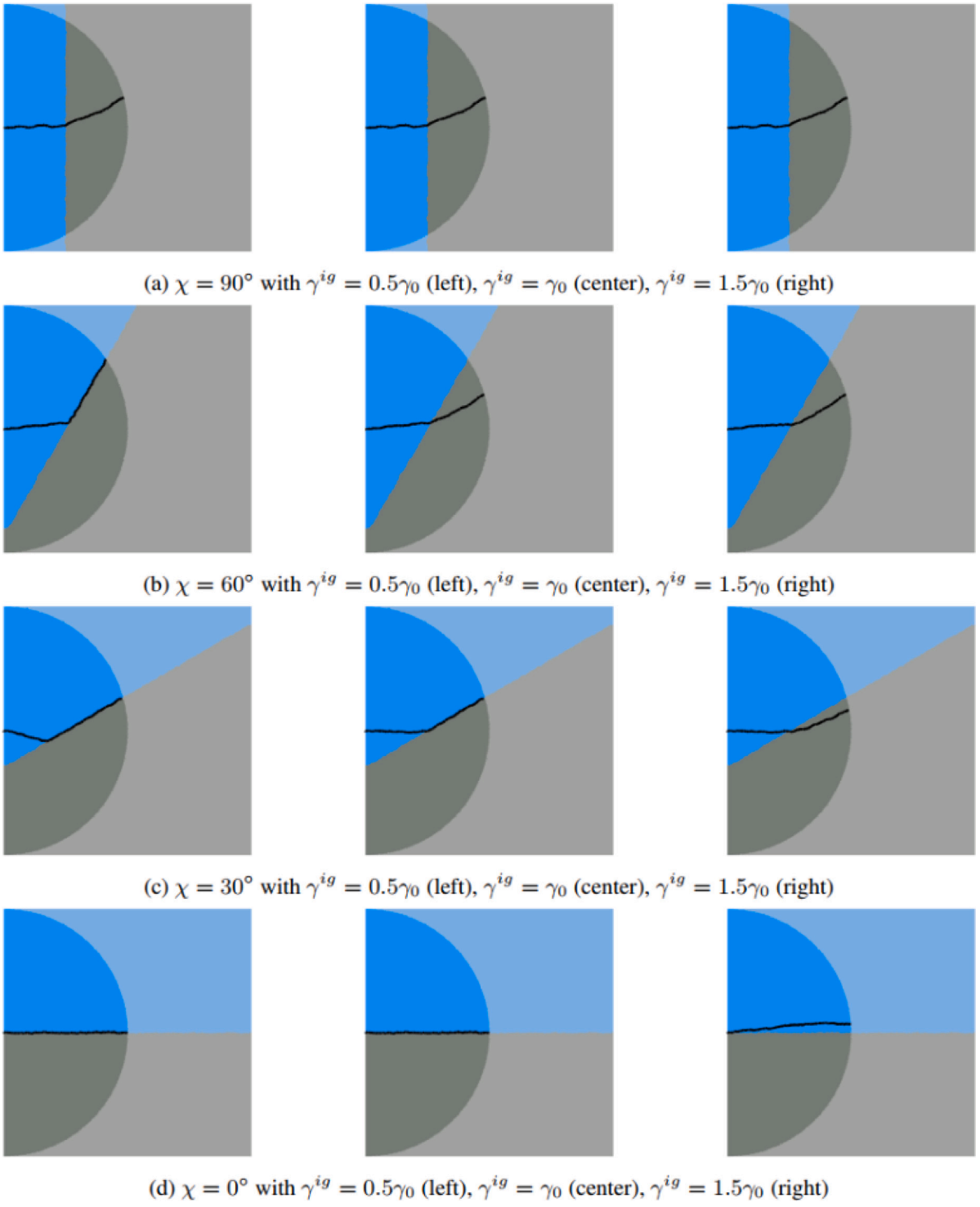

(a) $\chi = 90°$ with $\gamma^{ig} = 0.5\gamma_0$ (left), $\gamma^{ig} = \gamma_0$ (center), $\gamma^{ig} = 1.5\gamma_0$ (right)

(b) $\chi = 60°$ with $\gamma^{ig} = 0.5\gamma_0$ (left), $\gamma^{ig} = \gamma_0$ (center), $\gamma^{ig} = 1.5\gamma_0$ (right)

(c) $\chi = 30°$ with $\gamma^{ig} = 0.5\gamma_0$ (left), $\gamma^{ig} = \gamma_0$ (center), $\gamma^{ig} = 1.5\gamma_0$ (right)

(d) $\chi = 0°$ with $\gamma^{ig} = 0.5\gamma_0$ (left), $\gamma^{ig} = \gamma_0$ (center), $\gamma^{ig} = 1.5\gamma_0$ (right)

Fig. 13. Effect of grain boundary on crack propagation.

A similar analysis was conducted in [13], where a phase-field model was used to analyze intergranular and transgranular crack propagation in ZrB_2 bicrystal systems. It was observed that the crack path deviates from its initial trajectory before its incidence on the grain boundary. This behavior was more prominent for weaker grain boundaries. These observations are similar to the ones made in this work; however, the length-scale of these deviations is far smaller in the phase-field study.

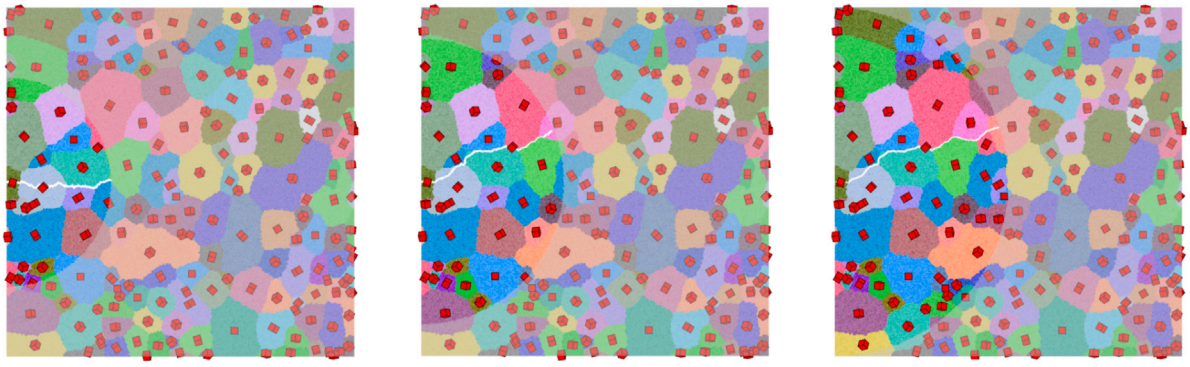

Fig. 14. Effect of $\bar{r}$ on crack path.

Table 3
Crack propagation angle in mixed-mode failure.

	Test - 1	Test - 2	Test - 3
$\frac{(\kappa+1)a\pi}{8\mu\gamma_0}\sigma_T^2$ (J/mm)	2.8	10.0	20.0
Microscopic surface energy (J)	1.36	1.41	1.43
Macroscopic energy release (J)	1.36	4.97	9.97
Total Energy (J)	0.00	−3.56	−8.54

4.2.2. Effect of macroscopic length scale

The macroscopic length scale is defined based on the choice of the parameter $\bar{r}$. A smaller choice of $\bar{r}$ implies a smaller macroscopic crack. If this parameter is chosen to represent a sub-grain length scale, then the estimated crack is expected to be closer to the corresponding homogeneous medium case. In contrast, if a larger value of $\bar{r}$ is chosen, then the predicted crack path will depend on the microstructure's spatial distribution. A thin foil specimen of polycrystalline material with cubic grains under the Mode-I tensile test is analyzed as the test case. The surface energy is determined by Eq. (10) with parameters: $\gamma_0 = 1$ J/mm^2 and $\delta = 2$. The intergranular surface energy density is taken as $\gamma^{ig} = 1$ J/mm^2, and the thickness of the specimen is taken as 1 mm. The crack path is estimated for 3 different values of $\bar{r}$ and the results are presented in Fig. 14. A prominently transgranular fracture in the macroscopically preferred direction is observed for the smallest value of $\bar{r}$. As the value of $\bar{r}$ is increased, the crack path converges towards a prominently intergranular fracture and moves away from the macroscopically preferred direction. It should be pointed out that this convergence is not guaranteed, for instance, in the specimens with large spatial variations in the microstructure's statistical features. For such cases, it is recommended to tune the hyperparameter, $\bar{r}$, using experimental studies.

4.2.3. Dynamic fracture

In previous examples, the value of σ_T was chosen such that the total energy of the crack was almost zero (i.e., $\varepsilon(\Gamma) \to 0^-$). This was done to emulate quasistatic crack growth conditions. In this section, the effect of the non-zero total energy of the crack is studied.

The test case is a thin foil specimen of cubic material with the same energy parameters as used in Section 4.2.2. The crack paths are predicted for three different values of σ_T, including the critical value, representing the quasistatic case. The values of σ_T and the resulting energies are presented in Table 3 and the predicted crack paths are shown in Fig. 15. It should be noted that the crack paths are dependent on the microstructure. For this particular choice of microstructure, it can be observed that: (1) The transgranular crack seems to follow the trace of [100] cleavage plane as expected. (2) In the critical case, an intergranular fracture is dominant, and the crack has a non-zero macroscopic angle. This macroscopic angle of the crack decreases in magnitude with increasing σ_T. It is observed from Table 3 that the total energy of the crack decreases with increasing tensile stress on the specimen. However, the total surface energy of the fractured surface increases with tensile stress. This result is expected as the increase in the energy release rate shifts the competition of the microscopic surface energy and macroscopic energy release in favor of the latter energy.

The second point in the revised ME Criterion hypothesis states that the crack propagation is possible in any loading condition, which satisfies $\varepsilon(\Gamma) < 0$. An elastodynamic extension to Griffith's fracture as presented in [37] showed that an equilibrium crack in-plane strain mode - I failure with finite velocity (v) has an augmented energy release rate ($\widetilde{G}$) given as: $\widetilde{G}(v, \alpha) = A(v)G(\alpha)$. In the limiting case of quasistatic fracture, the solution can be recovered from the finite velocity case as $\lim_{v\to 0^+} A(v) \to 1$. Similar results are available for Mode-II failure as well. This analysis qualitatively agrees with the hypothesis of this paper. Essentially, the cracked path in Mode-I dynamic fracture is likely to follow the cracked path as determined by the macroscopic conditions. Moreover, the crack velocity can be estimated by the ratio of macroscopic energy release of the dynamic crack and the respective quasistatic case.

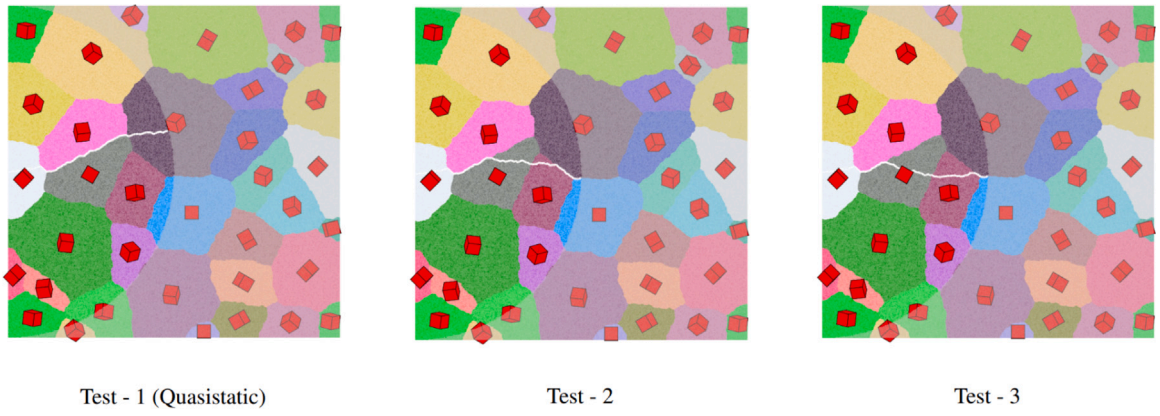

Fig. 15. Dynamic crack propagation in a polycrystalline material.

Further investigation is needed to verify this claim quantitatively. However, the rarity of experimental and analytical studies for microscopic dynamic growth in a polycrystalline material has prohibited the authors from doing so.

5. Conclusion

A graph-based approach is developed to predict the microscopic crack path during brittle fracture in a polycrystalline material. The method is based on an energy minimization principle with the crack's total energy as the cost. This approach naturally allows intergranular and transgranular fractures. The implementation presented in this paper specializes in macroscopically isotropic materials; however, it can be easily extended to the anisotropic case by considering the respective energy release rate. One major drawback of this procedure is mesh-dependence as the crack is only allowed to move along the mesh's edges. The present work uses a mesh generated by Delaunay triangulation of randomly sampled points. The final placement of edges is dependent on the sampled random points. However, it is observed from numerical simulations that the crack path from two different mesh has a minimal difference if the mesh is fine enough.

The accuracy of the outlined method is verified against analytical results of quasistatic fracture in homogeneous materials with different types of surface energy forms. In the case of isotropic surface energy, it was observed that the crack path appears to be radial with crack angles similar to those described by the ME-Criterion for mixed-mode failure. In case a single cleavage direction is present, the crack path is again radial and tends to follow the direction prescribed by a Geometric construction method provided by [36]. In the case of multiple cleavage directions, a transition from a smooth radial crack to a saw-tooth pattern is observed, as suggested by [36]. The effect of grain boundary energy is also studied, and the expected transition of intergranular to transgranular fracture is observed when the surface energy of the grain boundary is increased. While studying the effect of the grain boundary's incidence angle, it was observed that the crack path might be affected by the boundary ahead of the intergranular fracture. The reason for this effect is that when the intergranular surface energy is too low, then the global minimization of energy may lead to sub-optimal choice locally in the transgranular region. Meanwhile, the fracture's overall energy is decreased due to the generation of a longer intergranular surface. One contribution of this paper is in developing this approach for fracture in thin foil specimens by allowing the fractured surface to have a dihedral angle. This approach allows computing the 2D surface energy from the 3D crystal in a natural way. The simulations show that the cracked surface follows the cleavage plane's trace, as seen in many experimental studies. An unintended but favorable consequence of this formulation is that it allows for dynamic fracture as well. Simulations show that cracks with higher total energy tend to have a microscopic path which is macroscopically favorable but microscopically sub-optimal. This effect qualitatively makes sense but requires a rigorous verification with experimental or analytical studies.

The objective of this work is to introduce a graph-based procedure for estimating the microscopic crack path. The modularity of this procedure allows many possible modifications to the formalism of the fracture criterion. For instance, the ME Criterion used in this method is not suited for studying fracture due to compression. A possible remedy to this problem is to use the S-criterion, which can be implemented by replacing the energy release rate (G) with the negative of the strain energy density factor as introduced by [27]. Another possible extension of this method is the crack path prediction in ductile failure. In this case, the plastic strain energy can be included by augmenting the surface energy as $\gamma + \gamma_p$, as defined in [38]. The performance of these extensions will be addressed in subsequent works.

Declaration of competing interest

The authors declare that they have no known competing financial interests or personal relationships that could have appeared to influence the work reported in this paper.

Acknowledgments

The authors would like to acknowledge the Air Force Office of Scientific Research Materials for Extreme Environments Program (United States of America) (Grant No. FA9550-18-1-0091) for financial support on graph-theoretic modeling of microstructures. Additionally, the computations in this paper have been carried out as part of research infrastructure supported by the U.S. Department of Energy, Office of Basic Energy Sciences, Division of Materials Sciences and Engineering (Award No. DE-SC0008637) which funds the PRedictive Integrated Structural Materials Science (PRISMS) Center at the University of Michigan.

Appendix A. Definitions

Definition 1 (*FE Mesh*)**.** Given a closed bounded polyhedral domain $\Omega \in \mathbb{R}^3$, consider a finite partition $\mathcal{P}_h$ of Ω into polyhedrons P_i(indexed with i) such that

$$\Omega = \bigcup_{P_i \in \mathcal{P}_h} P_i$$

such that:

1. $int(P_i) \neq \phi \ \forall P_i \in \mathcal{P}_h$
2. $int(P_i) \cap int(P_j) = \phi \ \forall P_i, P_j \in \mathcal{P}_h$ s.t. $P_i \neq P_j$
3. if $F = P_i \cap P_j \neq \phi$ for some $P_i, P_j \in \mathcal{P}_h$ and $P_i \neq P_j$, then F is either a whole face (polygon), a whole edge (line segment), or a node (point) of the polygons P_i and P_j
4. $h = \max_{P_i \in \mathcal{P}} h_i$ where h_i denotes the longest euclidean distance between two points of P_i.

where $int(.)$ denotes the interior. The partition $\mathcal{P}_h$ is called the *mesh* of Ω.

Remarks: In the case of a 2D polygonal domain, $\Omega \in \mathbb{R}^2$, this definition can be extended by considering the partitions of polygons, P_i and modifying condition (3) to consider only edges and corners.

Definition 2 (*Graph and undirected graph*)**.** A graph (G) is a pair of sets (V, E), where V is the set of vertices and E is the set of edges/connections. For each element $e \in E$, there is an associated order pair (x, y) for some $x, y \in V$, i.e. $E \subseteq V \times V$. A Graph, $G = (V, E)$ is undirected if $(x, y) \in E \Rightarrow (y, x) \in E$ for all $x, y \in V$.

Remark: The term *connection* is preferred for graphs to avoid confusion with the edges of a mesh.

Appendix B. Proof of propositions

Proposition 1. *Given a straight crack at an angle α, defined as a mesh partition with label $+1$ in the upper sector and -1 in the lower sector, Eq. (6) holds true in the continuum limit of the mesh when g has the following form where $k < 2$:*

$$g(c_i, l_i) \equiv (2-k)\bar{r}^{k-1}\frac{\overline{g}(\theta_i, l_i)}{r_i^k}$$

Proof. Taking the continuum limit:

$$\begin{aligned}\lim_{h\to 0}\sum_{P_i \in \mathcal{P}_h}(2-k)\bar{r}^{k-1}\frac{\overline{g}(\theta_i, l_i)}{r_i^k}|P_i| &= \int_A (2-k)\bar{r}^{k-1}\frac{\overline{g}(\theta, l)}{r^k}dA \\ &= \int_{-\pi/2}^{\pi/2}\int_0^{\bar{r}}(2-k)\bar{r}^{k-1}\frac{\overline{g}(\theta, l)}{r^k}r\,dr\,d\theta \\ &= \bar{r}\int_{-\pi/2}^{\pi/2}\overline{g}(\theta, l)d\theta\end{aligned}$$

Choosing the labels as $l = 1$ when $\theta \in [\alpha, \pi/2]$ and $l = -1$ when $\theta \in [-\pi/2, \alpha)$ gets the desired result.

Proposition 2. *Eq. (7) satisfies Eq. (6)*

Proof. Taking derivative of Eq. (6) with respect to α on both sides:

$$\overline{g}(\alpha, +1) - \overline{g}(\alpha, -1) = G'(\alpha)$$

Clearly the form provided in Eq. (7) satisfies the above equation. The variable c can be estimated by substituting this form back in Eq. (6) and evaluating it for $\alpha = \pi/2$ to get:

$$c = \frac{1}{\pi}\left(-G(\pi/2) + \int_{-\pi/2}^{\pi/2} G'(\theta)H(-G'(\theta))d\theta\right)$$

Similarly, evaluating it for $\alpha = -\pi/2$ gives:

$$c = \frac{1}{\pi}\left(-G(-\pi/2) - \int_{-\pi/2}^{\pi/2} G'(\theta)H(G'(\theta))d\theta\right)$$

Note that both values are equal as:

$$G(\pi/2) - G(-\pi/2) = \int_{-\pi/2}^{\pi/2} G'(\theta)d\theta = \int_{-\pi/2}^{\pi/2} G'(\theta)(H(G'(\theta)) + H(-G'(\theta)))d\theta$$
$$\implies -G(-\pi/2) - \int_{-\pi/2}^{\pi/2} G'(\theta)H(G'(\theta))d\theta = -G(\pi/2) + \int_{-\pi/2}^{\pi/2} G'(\theta)H(-G'(\theta))d\theta$$

Proposition 3. *Given a rough crack represented using its angular position (α) as a function of the radial position, Eq. (9) holds in the continuum limit.*

Proof. As earlier, the crack is defined as a mesh partition with label $+1$ in the upper sector and -1 in the lower sector. Taking the continuum limit:

$$\begin{aligned}\lim_{h\to 0}\sum_{P_i\in\mathcal{P}_h} g(c_i,l_i)|P_i| &= \int_A (2-k)\bar{r}^{k-1}\frac{\overline{g}(\theta,l)}{r^k}dA \\ &= \int_0^{\bar{r}}\int_{-\pi/2}^{\pi/2}(2-k)\bar{r}^{k-1}\frac{\overline{g}(\theta,l)}{r^k}rd\theta dr \\ &= (2-k)\bar{r}^{k-1}\int_0^{\bar{r}}\frac{1}{r^{k-1}}\left(\int_{\alpha(r)}^{\pi/2}\overline{g}(\theta,+1)d\theta + \int_{-\pi/2}^{\alpha(r)}\overline{g}(\theta,-1)d\theta\right)dr\end{aligned}$$

Using Eq. (6),

$$\lim_{h\to 0}\sum_{P_i\in\mathcal{P}_h} g(c_i,l_i)|P_i| = (k-2)\bar{r}^k\int_0^{\bar{r}}\frac{1}{r^{k-1}}G(\alpha(r))dr$$

Normalizing the radial variable from r to $s = r/\bar{r}$,

$$\lim_{h\to 0}\sum_{P_i\in\mathcal{P}_h} g(c_i,l_i)|P_i| = (k-2)\bar{r}\int_0^1\frac{1}{s^{k-1}}G(\alpha(\bar{r}s))ds$$

Appendix C. Data structure and pseudocode

Here, the data structure used in the algorithm is presented. There are two kinds of data that are required in this algorithm: (1) FE Mesh data and (2) Image data. It is recommended to calculate and save all the variables as defined below at the time of mesh generation and be passed on to the mesh labeling algorithm.

FE Mesh Data: The basic structure for any FE Mesh includes following bare-bone data:

- *Nnode*: Number of nodes of the mesh
- *Coordinate*: Location of each node of the mesh
- *Nelement*: Number of elements
- *Connectivity*: Contains tuples with nodes of each element

It is post-processed to include the following derived quantities:

- *ElementCenter*: Coordinates of a point in the interior of the element (possibly centroid)
- *Neighbor*: It contains each pair of elements which share an edge.
- *Npair*: Number of Neighbors
- *ElementArea*: Area of each element
- *Edge*: It contains tuples with nodes of shared edges (indexed as the *Neighbor* data)
- *EdgeLength*: Length of each edge defined in *Edge* data
- *EdgeNormal*: Unit Normal of each edge defined in *Edge* data

Finally, the smooth labeling procedure [34] provides the *GrainID* of each element in the mesh, based on the experimental image.

Material Property Data: The Polycrystalline material properties are stored the form of the following variables:

- *GrainOrientation*: Axis-Angle representation for each value of GrainID
- *SurfaceEnergyParameter*: Surface energy parameters for each value of GrainID
- *ShearModulus*: Effective Shear Modulus of the specimen
- *PoissonRatio*: Effective Poisson's Ratio of the specimen
- *IntergranularEnergy*: γ^{ig} for each pair of grains

Next the basic Pseudocode modules are presented as used in 3.2:

Algorithm 1 Set-up Neighbor Cost

$M \leftarrow$ Mesh data ▷ Import mesh data
$P \leftarrow$ Material Property Data ▷ Import Material Property Data
$NC \leftarrow$ zeros($Nelement$) ▷ Initialize Smooth cost variable as a square matrix of zeros
$dihedral \leftarrow$ zeros($Npair$,1) ▷ Initialize Smooth cost variable as a square matrix of zeros
for $i \leftarrow 1$ to $M.Npair$ **do** ▷ Loop over all shared edges
  $Grain1 \leftarrow M.GrainID(M.Neighbor(i,1))$
  $Grain2 \leftarrow M.GrainID(M.Neighbor(i,2))$
  if $Grain1 == Grain2$ **then** ▷ Transgranular edge
    $dihedral(i) \leftarrow \psi_D$ (evaluated using Eq. (12))
    $SurfaceDensity \leftarrow \widetilde{\gamma}$ (evaluated using Eq. (13))
  else ▷ Intergranular edge
    $SurfaceDensity \leftarrow P.IntergranularEnergy(Grain1, Grain2)$
  end if
  $NC(M.Neighbor(i,1), M.Neighbor(i,2)) \leftarrow 2SurfaceDensity \times M.EdgeLength(i)$ ▷ Update Neighbor Cost
end for
return NC, $dihedral$

Algorithm 2 Set-up Data Cost

Input: $\bar{r}$, σ_T, β, a ▷ Input domain radius, Tensile stress, crack angle and length
$M \leftarrow$ Mesh data ▷ Import mesh data
$P \leftarrow$ Material Property Data ▷ Import Material Property Data
$K_I, K_{II} \leftarrow$ Evaluate Eq. (14) using argument β
$R\text{-}Index \leftarrow$ (distance($M.ElementCenter$,$Cracktip$)$< \bar{r}$) ▷ Index of elements within domain defined by $\bar{r}$
$(r_i, \theta_i)_{i \in R\text{-}Index}$ = cartesian2polar($M.ElementCenter\text{-}Cracktip$) ▷ Find Polar coordinate of each element
for i $\in R\text{-}Index$ **do**
  $G'(\theta_i) \leftarrow$ Evaluate Eq. (8) using arguments K_I, K_{II},$P.ShearModulus$ and $P.PoissonRatio$.
  $g(i,.) \leftarrow$ Evaluate Eq. (7)
  $DC_0(.,i) \leftarrow$ Evaluate Eq. (17) using arguments $g(i,.)$, r_i, $M.ElementArea(i)$
end for
$UpperBoundaryIndex \leftarrow$ ($M.ElementCenter \in$ UpperBoundary)
$LowerBoundaryIndex \leftarrow$ ($M.ElementCenter \in$ LowerBoundary)
DC_{BC}(2,$UpperBoundaryIndex$) $\leftarrow$ LargeNumber
DC_{BC}(1,$LowerBoundaryIndex$) $\leftarrow$ LargeNumber
return DC_0, DC_{BC},$R\text{-}Index$

Algorithm 3 Estimate Crack Path

Input: DC_0, DC_{BC}, NC, $R\text{-}Index$ ▷ Input variables
$h \leftarrow$ GCO_Create($NNodes$ = length(R-Index),NLabel=2)
GCO_SetDataCost($h, DC_0 + DC_{BC}$);
$LC \leftarrow$ ones(2) - Id(2)
GCO_SetSmoothCost(h, LC);
GCO_SetNeighbors($h, NC(R\text{-}Index, R\text{-}Index)$); ▷ Use Neighbor cost only for vertices in radial domain
GCO_Expansion(h);
$Label \leftarrow$ GCO_GetLabeling(h); ▷ This outputs label in {1,2} format. Change it to {+1,-1} format, if desired.
return $Label$

Algorithm 4 Evaluate total energy

Input: DC_0, NC, $Label$, $R\text{-}Index$
$EnergyRelease \leftarrow -\left(\sum_j DC(Label, j)\right)$
x $\leftarrow$ ($Label == 1$) ▷ TypeCast bool to float type for next calculation
y $\leftarrow$ ($Label == 2$) ▷ Or equivalently, $Label == -1$. TypeCast bool to float type
$NC_R \leftarrow NC(R\text{-}Index, R\text{-}Index)$ ▷ Use Neighbor cost only for vertices in radial domain
$SurfaceEnergy \leftarrow \sum_{ij} x_i y_j (NC_R)_{ij}$
return $\varepsilon(\Gamma) \leftarrow SurfaceEnergy$ - $EnergyRelease$

References

[1] Boykov Y, Veksler O, Zabih R. Fast approximate energy minimization via graph cuts. IEEE Trans Pattern Anal Mach Intell 2001;23(11):1222–39, https://doi.org/10.1109/cvpr.2010.5539897.
[2] Ushijima-Mwesigwa H, Negre CFA, Mniszewski SM. Graph partitioning using quantum annealing on the D-Wave system. In: Proceedings of the second international workshop on post moores era supercomputing. 2017. p. 22–29.
[3] Kelly A, Tyson WR, Cottrell AH. Ductile and brittle crystals. Phil Mag A 1967;15(135):567–86.
[4] Ortiz M, Pandolfi A. Finite-deformation irreversible cohesive elements for three-dimensional crack-propagation analysis. Internat J Numer Methods Engrg 1999;44(9):1267–82.
[5] Simonovski I, Cizelj L. Cohesive zone modeling of intergranular cracking in polycrystalline aggregates. Nucl Eng Des 2015;283:139–47.
[6] Samimi M, Van Dommelen JAW, Geers MGD. An enriched cohesive zone model for delamination in brittle interfaces. Internat J Numer Methods Engrg 2009;80(5):609–30.
[7] Li Y, McDowell DL, Zhou M. A multiscale framework for predicting fracture toughness of polycrystalline metals. Mater Perform Characteriz 2014;3(3):157–72. http://dx.doi.org/10.1520/MPC20130064.
[8] Gao YF, Bower AF. A simple technique for avoiding convergence problems in finite element simulations of crack nucleation and growth on cohesive interfaces. Modelling Simulation Mater Sci Eng 2004;12(3):453.
[9] Kuhn C, Müller R. A continuum phase field model for fracture. Eng Fract Mech 2010;77(18):3625–34.
[10] Hakim V, Karma A. Laws of crack motion and phase-field models of fracture. J Mech Phys Solids 2009;57(2):342–68.
[11] Miehe C, Welschinger F, Hofacker M. Thermodynamically consistent phase-field models of fracture: Variational principles and multi-field FE implementations. Internat J Numer Methods Engrg 2010;83(10):1273–311.
[12] Murakami S, Liu Y. Mesh-dependence in local approach to creep fracture. Int J Damage Mech 1995;4(3):230–50.
[13] Emdadi A, Asle Zaeem M. Phase-field modeling of crack propagation in polycrystalline materials. Comput Mater Sci 2021;186:110057. http://dx.doi.org/10.1016/j.commatsci.2020.110057, http://www.sciencedirect.com/science/article/pii/S0927025620305486.
[14] Moës N, Dolbow J, Belytschko T. A finite element method for crack growth without remeshing. Internat J Numer Methods Engrg 1999;46(1):131–50.
[15] Oliver J, Huespe AE, Sánchez PJ. A comparative study on finite elements for capturing strong discontinuities: E-FEM vs X-FEM. Comput Methods Appl Mech Engrg 2006;195(37–40):4732–52.
[16] Panwar S, Sun S, Sundararaghavan V. Modeling fatigue failure using the variational multiscale method. Eng Fract Mech 2016;162:290–308.
[17] Francfort GA, Marigo J-J. Revisiting brittle fracture as an energy minimization problem. J Mech Phys Solids 1998;46(8):1319–42.
[18] Adams J. Investigating microstructural effects on short crack growth and fatigue life behavior of WE43 magnesium. 2018, University of Michigan, Ann Arbor.
[19] Sundararaghavan V, Srivastava S. Microfract: An image based code for microstructural crack path prediction. SoftwareX 2017;6:94–7, https://doi.org/10.1016/j.softx.2017.04.002.
[20] Srinivasan G, Hyman JD, Osthus DA, Moore BA, O'Malley D, Karra S, Rougier E, Hagberg AA, Hunter A, Viswanathan HS. Quantifying topological uncertainty in fractured systems using graph theory and machine learning. Sci Rep 2018;8(1):1–11.
[21] Hunter A, Moore BA, Mudunuru M, Chau V, Tchoua R, Nyshadham C, Karra S, O'Malley D, Rougier E, Viswanathan H, et al. Reduced-order modeling through machine learning and graph-theoretic approaches for brittle fracture applications. Comput Mater Sci 2019;157:87–98.
[22] Bock FE, Aydin RC, Cyron CJ, Huber N, Kalidindi SR, Klusemann B. A review of the application of machine learning and data mining approaches in continuum materials mechanics. Front Mater 2019;6:110. http://dx.doi.org/10.3389/fmats.2019.00110, https://www.frontiersin.org/article/10.3389/fmats.2019.00110.
[23] Osovski S, Needleman A, Srivastava A. Intergranular fracture prediction and microstructure design. Int J Fract 2019;216(2):135–48.
[24] Molkeri A, Srivastava A, Osovski S, Needleman A. Influence of grain size distribution on ductile intergranular crack growth resistance. J Appl Mech 2019;87(3):031008. http://dx.doi.org/10.1115/1.4045073, arXiv:https://asmedigitalcollection.asme.org/appliedmechanics/article-pdf/87/3/031008/6482889/jam_87_3_031008.pdf.
[25] Kolmogorov V, Zabin R. What energy functions can be minimized via graph cuts? IEEE Trans Pattern Anal Mach Intell 2004;26(2):147–59.
[26] Boykov Y, Kolmogorov V. An experimental comparison of min-cut/max- flow algorithms for energy minimization in vision. IEEE Trans Pattern Anal Mach Intell 2004;26(9):1124–37.
[27] Sih GC. Strain-energy-density factor applied to mixed mode crack problems. Int J Fract 1974;10(3):305–21.
[28] Sih GC. Mechanics of fracture initiation and propagation: surface and volume energy density applied as failure criterion, vol. 11. Springer Science & Business Media; 2012.
[29] Nuismer RJ. An energy release rate criterion for mixed mode fracture. Int J Fract 1975;11(2):245–50.
[30] Palaniswamy K. Crack propagation under general in-plane loading. 1972, California Institute of Technology.
[31] Erdogan F, Sih GC. On the crack extension in plates under plane loading and transverse shear. J Basic Eng 1963;85(4):519–25. http://dx.doi.org/10.1115/1.3656897, arXiv:https://asmedigitalcollection.asme.org/fluidsengineering/article-pdf/85/4/519/5763775/519_1.pdf.
[32] Azhdari A, Nemat-Nasser S. Energy-release rate and crack kinking in anisotropic brittle solids. J Mech Phys Solids 1996;44(6):929–51.
[33] Teichtmeister S, Kienle D, Aldakheel F, Keip M-A. Phase field modeling of fracture in anisotropic brittle solids. Int J Non-Linear Mech 2017;97:1–21.
[34] Srivastava S, Sundararaghavan V. Graph coloring approach to mesh generation in multiphase media with smooth boundaries. AIAA J 2020;58(1):198–205.
[35] Schmidt FR, Toppe E, Cremers D. Efficient planar graph cuts with applications in Computer Vision. In: 2009 IEEE conference on computer vision and pattern recognition. 2009. p. 351–356.
[36] Takei A, Roman B, Bico J, Hamm E, Melo F. Forbidden directions for the fracture of thin anisotropic sheets: an analogy with the wulff plot. Phys Rev Lett 2013;110(14):144301.
[37] Freund LB. Energy concepts in dynamic fracture. In: Dynamic fracture mechanics. Cambridge monographs on mechanics, Cambridge University Press; 1990, p. 221–95. http://dx.doi.org/10.1017/CBO9780511546761.006.
[38] Orowan E. Fracture and strength of solids. Rep Prog Phys 1949;12(1):185.